3D experimental and computational analysis of eccentric mitral regurgitant jets in a mock imaging heart chamber

Y. WANG   A. QUAINI   S. ČANIĆ   S. H. LITTLE
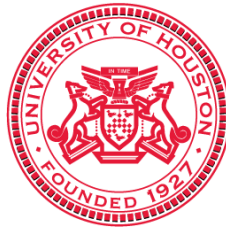
3D experimental and computational analysis of eccentric mitral regurgitant jets in a mock imaging heart chamber

Yifan Wang[,b], Annalisa Quaini[b], Sunčica Čanić[b], Stephen H. Little[a]

[a] The Methodist Hospital Houston, 6550 Fannin Suite 1901, Houston
[b] Department of Mathematics, University of Houston, 4800 Calhoun Rd, Houston TX 77204, USA

Abstract

Mitral valve regurgitation (MR) is a disorder of the heart in which the mitral valve does not close properly. This causes an abnormal leaking of blood backwards from the left ventricle into the left atrium during the systolic contractions of the left ventricle. Noninvasive assessment of MR using echocardiography is an ongoing challenge. In particular, a major problem are eccentric or Coanda regurgitant jets which hug the walls of the left atrium and appear smaller in the color Doppler image of regurgitant flow. This manuscript presents a comprehensive investigation of Coanda regurgitant jets and the associated intracardiac flows by using a combination of experimental and computational approaches. An anatomically correct mock heart chamber connected to a pulsatile flow loop is used to generate the physiologically relevant flow conditions, and the influence of two clinically relevant parameters (orifice aspect ratio and regurgitant volume) on the onset of Coanda effect is studied. A two parameter bifurcation diagram showing transition to Coanda jets is obtained, indicating that: (1) strong wall hugging jets occur in long and narrow orifices with moderate to large regurgitant volumes, and (2) short orifices with moderate to large regurgitant volumes produce strong 3D flow features such as vortex rolls, giving rise to the velocities that are orthogonal to the 2D plane associated with the apical color Doppler views, making them "invisible" to the single plane color Doppler assessment of MR. This is the first work in which the presence of vortex rolls in the left atrium during regurgitation is reported and identified as one of the reasons for under-estimation of regurgitant volume. The results of this work can be used for better design of imaging strategies in noninvasive assessment of MR, and for better understanding of LA remodeling that may be associated with the presence of maladapted vortex dynamics. This introduces a new concept in clinical imaging, which emphasizes that the *quality* and not only the *quantity* of regurgitant flow matters in the assessment of severity of mitral valve regurgitation.

Key words: Mitral valve regurgitation, echocardiography, Coanda effect.

1. Introduction

Mitral valve regurgitation (MR) is a disorder of the heart in which the mitral valve does not close properly. This causes an abnormal leaking of blood backwards from the left ventricle, through

the mitral valve, into the left atrium during the systolic contractions of the left ventricle. MR is the most common form of valvular heart disease [25]. Mitral valve regurgitation can lead to atrial

(a) Central regurgitant jet   (b) Eccentric regurgitant jet
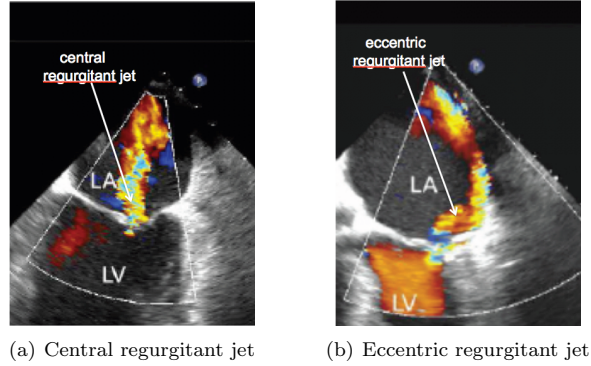
Figure 1: 2D color Doppler image of (a) central regurgitant jet flowing from the left ventricle (LV) to the left atrium (LA) and (b) eccentric regurgitant jet known as Coanda effect, hugging the walls of the left atrium.

arrhythmias, pulmonary artery hypertension, congestive heart failure and death. The decision to proceed with surgical valve repair or replacement is based on an assessment of symptoms and valve regurgitation severity. The primary tool to assess the severity of MR is echocardiography [42, 24, 16]. Color Doppler imaging is used to provide a color display of blood flow direction and velocity within an area sampled by pulse-wave Doppler. This "map" of blood flow velocities is used to quantify MR severity. However, because these color Doppler displays represent velocities, and not regurgitant volume (RV) of blood, there are significant, although often unrecognized, limitations to their use. All color Doppler maps are subject to image angle limitations. Moreover, the magnitude and rate of blood pressure change can profoundly affect these velocity displays. Despite the publication of extensive guidelines by the American Society of Echocardiography [42, 24], accurate and reproducible assessment of regurgitant volume (RV) using echocardiography is an ongoing challenge [20].
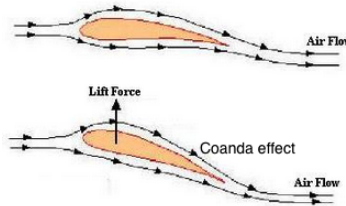
Figure 2: Coanda effect in aerodynamics. The figure shows a cross-section of a wing (in orange) and airflow (streamlines) around the wing at two different "attack angles". The hugging of the wing by the airflow jet, i.e., Coanda effect, is partially responsible for lift in aerodynamics. The stronger the Coanda effect, the stronger the lift (bottom figure).

The main challenges stem from estimating RV in eccentric regurgitant jets. Fig. 1(a) shows an example of a 2D color Doppler image of a central jet, i.e. a regurgitant jet located in the center

| (a) Flow loop | (b) 3D rendering of the chamber |
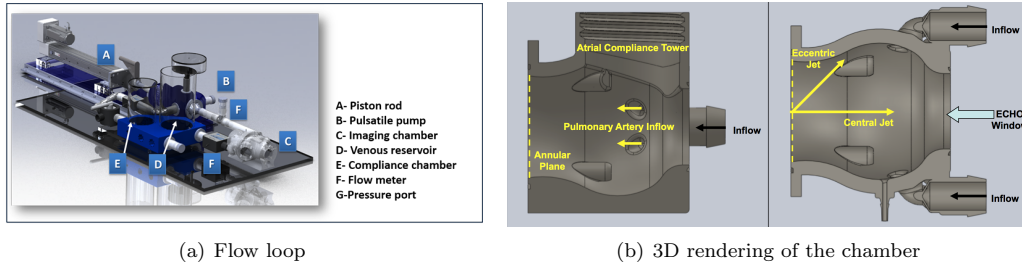
Figure 3: (a) Pulsatile flow loop containing the mock heart chamber and (b) 3D rendering of the mock heart chamber. In subfigure (b) we see: left atrium (a), pulmonary veins (b), ultrasound windows (c, f, h), leaky valve (d), left ventricle (e), ascending aorta (g).

of the left atrium, while Fig. 1(b) shows a 2D color Doppler image of an eccentric jet, i.e., a jet which "hugs" the mitral leaflet and atrial wall. Eccentric jets are known in echocardiography as *Coanda jets*, i.e., the jets undergoing *Coanda effect*, a phenomenon that is described in the scientific literature as the tendency of a fluid jet to be attracted to the nearby surface [39, 41]. The principle was named after Romanian aerodynamicist Henri Coanda, who was the first to recognize its practical application in airplane lift design in 1910. See Fig. 2. Only recently Coanda effect was recognized as one of the biggest challenges in echocardiographic assessment of mitral regurgitation: the eccentric, wall-hugging, non-symmetric regurgitant jets appear smaller in the color Doppler image of regurgitant flow than the central jets with the same regurgitant volume [42, 11]. This may lead to a gross under-estimation of regurgitant volume by inexperienced cardiovascular observers [11, 3]. As a result, patients who may need medical or surgical therapy may be left untreated.

Despite the large cardiovascular and bioengineering literature reporting on the Coanda effect in echocardiographic assessment of mitral regurgitation, there is very little connection with the fluid dynamics literature that could help identify and understand the complex flow features during mitral valve regurgitation and how they influence color Doppler assessment of MR. In this paper, we make a first step in this direction by carefully investigating the flow conditions in an anatomically correct mock imaging heart chamber simulating the flow conditions during systole when the flow regurgitates from the left ventricle to the left atrium across a regurgitant mitral valve. Our study combines the mathematical (computational) and experimental approaches.

Our experimental studies were performed on an anatomically correct mock (left) heart chamber developed at the Houston Methodist DeBakey Heart & Vascular Center [18] to study the use of 2D and 3D color Doppler techniques in imaging the clinically relevant complex intra-cardiac flow events associated with MR jets [18, 19]. See Figure 3(b). The chamber consists of a mock left ventricle and a mock left atrium which are connected through an orifice mimicking a regurgitant mitral valve. Details of the interior of the mock heart chamber are shown in Sec. 4 in Fig. 11. The chamber is connected to a pulsatile flow loop shown in Figure 3(a).

We investigated the influence of two clinically relevant parameters: the orifice aspect ratio (OAR), and regurgitant volume (RV), on the flow conditions in the left atrium, and on the estimation of severity of MR using 2D color Doppler echocardiography. We focused on eccentric regurgitant jets. The two clinically relevant parameters can be associated with two mathematically relevant flow parameters (non-dimensional parameters): the orifice aspect ratio (OAR) and the Reynolds number (Re). To obtain the detailed flow velocity field in the mock heart chamber,

3

and regurgitant volume, we utilized computational fluid dynamics. All the computational results presented in this article have been performed using LifeV [1], an open source library of algorithms and data structures for the numerical solution of partial differential equations with high performance computing techniques. In [27, 2], the Navier-Stokes solver used in this paper was successfully validated by the authors against experimental data up to Reynolds number 5000, which includes turbulent flows. In our previous works [31, 30], we showed that, once validated, computational models provide detailed, point-wise information about the quantities that are used in echocardiographic assessment of MR, thereby providing information that can be used to tune and refine the already existing diagnostic imaging protocols, or to design new protocols.

Using this software we first investigated flow conditions in a 2D contraction-expansion channel that lead to Coanda effect in 2D. More precisely, the 2D contraction-expansion channel consists of two rectangular chambers separated by a contraction mimicking an orifice. See Fig. 4(a). For a given aspect ratio of the channel, we investigated how an increase in the Reynolds number influences the transition from a central jet to an eccentric, Coanda jet. A bifurcation diagram describing the onset of Coanda effect is obtained. This is presented in Sec. 3.1. These results were compared with the already existing results in literature, showing excellent agreement [32]. This was an additional validation of our computer simulations applied to studying flows through contraction-expansion channels.

Next, we designed the corresponding 3D symmetric contraction-expansion channel and studied the influence of the third dimension on the formation of Coanda effect. This is presented in Sec. 3.2.

The 3D results in the stylized 3D contraction-expansion channel were then used as a guidance to study the flow conditions in the anatomically correct 3D mock heart chamber consisting of two sub-chambers, the anatomically correct left ventricle and the left atrium, separated by an orifice mimicking a regurgitant mitral valve. We studied the influence of regurgitant volume and orifice aspect ratio on the formation of Coanda effect in the anatomically correct left atrium, and analyzed the detailed intra-cardiac velocity vector field and how it influences 2D color Doppler assessment of MR. The results of this study are presented in Sec. 4. Various mathematically and clinically relevant conclusions were obtained. We show, among other things, that Coanda effect in the left ventricle occurs for orifices with larger aspect ratios (e.g., width:length=1:10) and larger regurgitant volumes (e.g., RV = 31 ml/beat). Furthermore, we show that orifices with smaller aspect ratio (e.g., width:length= 1:3.3 or 1:2.5) and larger regurgitant volumes (e.g., RV = 31 ml/beat) generate flows in the left atrium with significantly more pronounced 3D flow features than orifices with larger aspect ratio. In those situations doughnut-shaped vortex rolls appear at the end of the regurgitant jet, influencing the flow in the entire left atrium. The strong 3D features of such flows give rise to velocities orthogonal to the 2D plane associated with the apical color Doppler views. This makes large portions of the flow "invisible" to the single plane color Doppler assessment of RV, giving rise to under-estimation of the regurgitant jet area. This is the first work in which the presence of vortex rolls in the left atrium during regurgitation is reported and identified as one of the reasons for under-estimation of regurgitant volume. While the role of vortex dynamics in the *left ventricle* has been studied by several authors, see e.g., [10, 28], the role of vortex dynamics in the left atrium during regurgitation is, however, completely unexplored. The results of this work can be used for better design of imaging strategies in noninvasive assessment of MR, and for better understanding of LA remodeling that may be associated with the presence of maladapted vortex dynamics in the left atrium. Thus, we are introducing a new concept in clinical imaging, which emphasizes that the *quality* and not only the *quantity* of regurgitant flow matters in the assessment of severity of mitral valve regurgitation.

4

2. Problem definition

The motion of an incompressible viscous fluid in a spatial domain Ω over a time interval of interest $(0, T)$ is described by the Navier-Stokes equations

$$\rho \left(\frac{\partial \boldsymbol{u}}{\partial t} + (\boldsymbol{u} \cdot \nabla) \boldsymbol{u} \right) - \nabla \cdot \boldsymbol{\sigma} = \boldsymbol{f} \qquad \text{in } \Omega \times (0, T), \qquad (1)$$

$$\nabla \cdot \boldsymbol{u} = 0 \qquad \text{in } \Omega \times (0, T), \qquad (2)$$

where ρ is the fluid density, $\boldsymbol{u}$ is the fluid velocity, $\boldsymbol{\sigma}$ the Cauchy stress tensor and $\boldsymbol{f}$ the body force. For Newtonian fluids $\boldsymbol{\sigma}$ has the following expression

$$\boldsymbol{\sigma}(\boldsymbol{u}, p) = -p\mathbf{I} + 2\mu\boldsymbol{\epsilon}(\boldsymbol{u}),$$

where p is the pressure, μ is the fluid dynamic viscosity, and $\boldsymbol{\epsilon}(\boldsymbol{u}) = (\nabla \boldsymbol{u} + (\nabla \boldsymbol{u})^T)/2$ is the strain rate tensor. Equations (1)-(2) need to be supplemented with initial and boundary conditions:

$$\boldsymbol{u} = \boldsymbol{u}_D \text{ on } \partial\Omega_D \times (0, T), \qquad (3)$$

$$\boldsymbol{\sigma} \cdot \boldsymbol{n} = \boldsymbol{g} \quad \text{ on } \partial\Omega_N \times (0, T), \qquad (4)$$

$$\boldsymbol{u} = \boldsymbol{u}_0 \quad \text{ in } \Omega \times \{0\},$$

where $\overline{\partial\Omega_D} \cup \overline{\partial\Omega_N} = \overline{\partial\Omega}$ and $\partial\Omega_D \cap \partial\Omega_N = \emptyset$.

The Reynolds number can be used to characterize the flow regime. We define the Reynolds number as

$$Re = \frac{UL}{\nu} \qquad (5)$$

where U is a characteristic velocity within a geometry of characteristic length L (usually, hydraulic diameter) and $\nu = \mu/\rho$ is the fluid kynematic viscosity. The Reynolds number can be thought of as the ratio of inertial forces to viscous forces. For large Reynolds numbers, inertial forces are dominant over viscous forces and vice versa.

2.1. Discretization

We approximate in time equations (1)-(2) by the backward differentiation formula of order 2 (BDF2 [33]) and we linearize the convective term by an extrapolation formula of the same order. Given $\Delta t \in \mathbb{R}$, let us set $t^n = n\Delta t$, with $n = 0, ..., N_T$ and $T = N_T \Delta t$. Problem (1)-(2) discretized in time reads: given $\boldsymbol{u}^n$, for $n \geq 1$, find the solution $(\boldsymbol{u}^{n+1}, p^{n+1})$ of the system:

$$\rho \frac{3\boldsymbol{u}^{n+1} - 4\boldsymbol{u}^n + \boldsymbol{u}^{n-1}}{2\Delta t} + \rho(2\boldsymbol{u}^n - \boldsymbol{u}^{n-1}) \cdot \nabla \boldsymbol{u}^{n+1} - \nabla \cdot \boldsymbol{\sigma}(\boldsymbol{u}^{n+1}, p^{n+1}) = \mathbf{0} \qquad \text{in } \Omega, \quad (6)$$

$$\nabla \cdot \boldsymbol{u}^{n+1} = 0 \qquad \text{in } \Omega. \quad (7)$$

For the space discretization, we introduce a conformal and quasi-uniform partition $\mathcal{T}_h$ of Ω made up of a certain number of tetrahedra. Since we use direct numerical simulations (DNS), it is essential that the flow field is properly resolved, i.e. $\mathcal{T}_h$ is sufficiently refined. We will use inf-sup stable finite element pair $\mathbb{P}_2$-$\mathbb{P}_1$. For more details concerning the discretization of the Navier-Stokes problem, we refer, e.g., to [36]. Even though the semi-implicit treatment of the convective term in eq. (6) does not guarantee the unconditional stability in time of the numerical scheme,

careful selection of time step and mesh size yields stable solutions without the need for numerical stabilization techniques. Thus, we do not use any stabilization for the convective term.

Let us denote by M the mass matrix, K the diffusion matrix, N the matrix associated with the discretization of the convective term, and B the matrix associated with the discretization of the operator $(-\nabla \cdot)$. The linearization and full discretization of problem (1)-(2) yields the following system

$$\rho \frac{3}{2\Delta t} M \mathbf{u}^{n+1} + \mu K \mathbf{u}^{n+1} + \rho N \mathbf{u}^{n+1} + B^T \mathbf{p}^{n+1} = \mathbf{b}_u^{n+1}, \tag{8}$$

$$B \mathbf{u}^{n+1} = \mathbf{0}, \tag{9}$$

where $\mathbf{u}^{n+1}$ and $\mathbf{p}^{n+1}$ are the arrays of nodal values for velocity and pressure. The array $\mathbf{b}_u^{n+1}$ accounts for the contributions of solution at the previous time steps and the contribution that the boundary nodes give to the internal nodes.

Set $C = \rho \frac{3}{2\Delta t} M + \mu K + \rho N$. We can rewrite (8)-(9) in the form

$$A \mathbf{x}^{n+1} = \mathbf{b}^{n+1}, \tag{10}$$

where

$$A = \left[\begin{array}{cc} C & B^T \\ B & 0 \end{array} \right], \quad \mathbf{x}^{n+1} = \left[\begin{array}{c} \mathbf{u}^{n+1} \\ \mathbf{p}^{n+1} \end{array} \right], \quad \mathbf{b}^{n+1} = \left[\begin{array}{c} \mathbf{b}_u^{n+1} \\ \mathbf{0} \end{array} \right]. \tag{11}$$

At every time level t^{n+1}, to solve system (10) we use the left preconditioned GMRES method. As preconditioner, we use an upper-triangular variant of the pressure corrected Yosida splitting [8, 38] given by

$$P = \left[\begin{array}{cc} C & B^T \\ 0 & S(S + BH(\mu K + \rho N)HB^T)^{-1}S \end{array} \right], \quad H = \frac{2\Delta t}{3\rho} M^{-1}, \quad S = -BHB^T. \tag{12}$$

See also [34, 35, 9] for more details.

The Navier-Stoker solver described in this section is implemented in LifeV and it is validated up to Reynolds number 5000 [27, 2]. The validation showed that a properly refined mesh is able to capture accurately the average flow features observed in the experiments performed by the U.S. Food and Drug Administration [13].

3. The Coanda effect in contraction-expansion channels

To better understand the mechanisms that are responsible to the onset of Coanda effect in the human heart, we first consider the flow through a "stylized" contraction-expansion channel in 2D and 3D, see Fig. 4. The contraction-expansion channels consist of an inlet chamber, a contraction, and an expansion (outlet) chamber. The flow enters thorough Γ_{in} into the inlet chamber, passes through the contraction, and exists through the expansion chamber and the boundary Γ_{out} located far downstream from the contraction. As we shall see below, different aspect ratios of the important geometric parameters, and different flow conditions described by the Reynolds number, give rise to different flow patterns in the expansion chamber, including Coanda effect. The important geometric parameters are:

- w–contraction width

- W–expansion chamber width

- H–expansion-contraction channel depth in 3D.

The purpose of this section is two-fold: one is to show the sequence of events that leads to Coanda effect, and the corresponding flow conditions in the expansion chamber as the Reynolds number increases, and the other is to validate our solver against the results reported in [26].

(a) 2D geometry   (b) 3D geometry
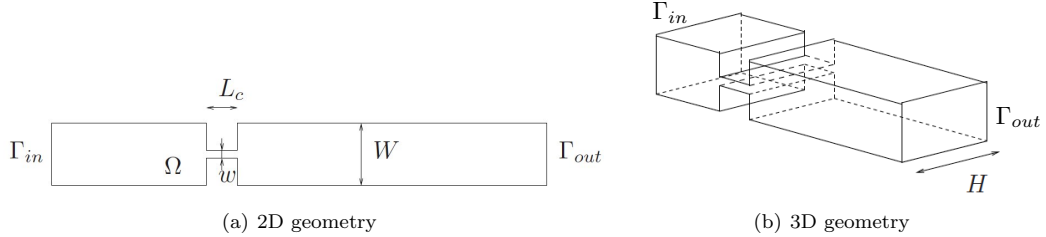
Figure 4: (a) 2D and (b) 3D contraction-expansion channel.

Our flow simulations were performed by supplementing Eqs. (1)-(2) with the following boundary conditions: parabolic velocity profile at the inlet Γ_{in}, stress-free boundary condition at the outlet Γ_{out}, and the no-slip condition on the rest of the boundary. The chamber upstream of the contraction and the expansion chamber need to be long enough so that the flow is fully established when it reaches both the contraction and the outlet section. We made sure that this was the case, as explained in e.g. [32]. The fluid is initially at rest. A time marching algorithm is used to approach the steady-state solution.

3.1. The 2D symmetric chamber

The flow in the 2D geometry shown in Fig. 4(a) can be seen as the limiting case of a 3D flow in the domain shown in Fig. 4(b) for channel depth H tending to infinity. For the 3D problem, the characteristic length L is given by the hydraulic diameter of the contraction channel, i.e. $L = 2Hw/(H+w)$, thus the corresponding Reynolds number (5) for the 3D contraction-expansions channel is given by:

$$Re_{3D} = \frac{\rho U}{\mu} \frac{2Hw}{H+w}. \tag{13}$$

By letting $H \to \infty$ in eq. (13), we define the Reynolds number for the corresponding 2D problem

$$Re_{2D} = 2\frac{\rho U w}{\mu}. \tag{14}$$

For characteristic velocity U in (14), we take the average velocity in the contraction channel. So, if we denote by $U_{\max}$ the maximum velocity in the contraction channel and assume that the contraction channel is long enough to have a fully developed parabolic velocity profile, we have $U = 2U_{\max}/3$. In the numerical simulations, we set $U_{\max} = 1$ and we change the value of the viscosity to achieve different Reynolds number flow regimes.

The geometry under consideration in [26] has upstream and downstream channel width $W = 4$, and contraction width $w = 0.26$. Thus, the expansion ratio $\lambda = W/w$ is 15.4. The length of the

contraction L_c is set to 2. In this domain, we simulate the flow for different Reynolds numbers (ranging from 0.01 to 71.3) to examine the onset of the Coanda effect.

In Fig. 5, we report the streamlines for the flow at four different values of Re_{2D}. For sufficiently small value of Re_{2D} (e.g., 0.01) a steady symmetric flow is observed. Moffatt eddies form (see [23]) close to the corners both upstream of the contraction and downstream of the expansion. See Fig. 5(a). As the inertia effects of fluid become more important, the Moffatt eddies upstream of the contraction gradually diminish in size and two recirculation regions of equal size develop downstream of the contraction. We see in Fig. 5(b) that the flow at $Re_{2D} = 7.8$ has lost the symmetry about the vertical axis, while the symmetry about the horizontal axis is maintained. As the Reynolds number increases, flow symmetry about the central line is initially maintained (see [7, 4]), while above a certain critical Reynolds number denoted by Re_{sb}, a steady asymmetric solution is observed (see [6, 37]). As we see in Fig. 5(c), which corresponds to $Re_{2D} = 31.1$, one downstream recirculation zone expands while the other shrinks.

(a) $Re_{2D} = 0.01$ (b) $Re_{2D} = 7.8$ (c) $Re_{2D} = 31.1$
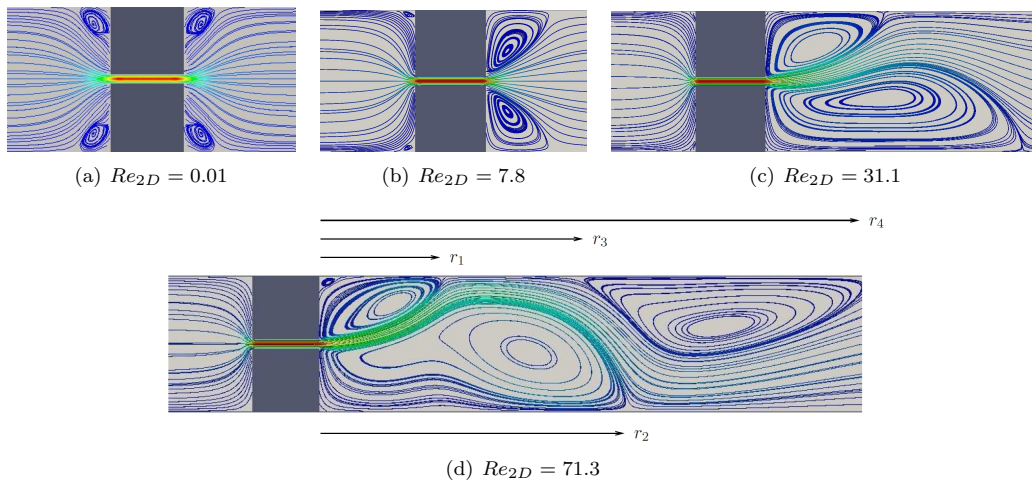
(d) $Re_{2D} = 71.3$

Figure 5: 2D contraction-expansion channel, expansion ratio $\lambda = 15.4$: streamlines for the flow at Reynolds numbers (a) $Re_{2D} = 0.01$, (b) $Re_{2D} = 7.8$, (c) $Re_{2D} = 31.1$, and (d) $Re_{2D} = 71.3$. The streamlines are colored with the velocity magnitude, with blue corresponding to 0 and red corresponding to 1.

This asymmetric solution remains stable for a certain range of Re_{2D} and asymmetries become stronger with the increasing Reynolds number, as shown in [22]. The formation of stable asymmetric vortices in 2D planar expansion is attributed to the Coanda effect (see [41]): an increase in velocity near one wall will lead to a decrease in pressure near that wall and once a pressure difference is established across the channel it will maintain the asymmetry of the flow.

Reference [14] explains the loss of symmetric stability as a result of the interaction between the effects of viscous dissipation, the downstream convection of perturbations by the base symmetric flow, and the upstream convection induced by 2D asymmetric disturbances. The small perturbations will lead to one of two possible asymmetric solutions, which are the reflected image of each other with respect to the domain symmetry axis.

The value Re_{sb} of the Reynolds number for which the flow loses symmetry has been identified for different expansion ratios λ. In particular, it was found that Re_{sb} decreases with increasing

8

value of λ (see [6, 37, 32]).

A further increase in Reynolds number generates a third vortex downstream on the side of the smaller primary vortex, as the enlarged one grows and pushes the jet even closer to the wall; see Fig. 5(d).

Fig. 5 is in good qualitative agreement with [26]. For a quantitative agreement, we report the bifurcation diagram in Fig. 6, which shows the effect of Reynolds number on the length of the recirculation zones formed downstream of the expansion. This bifurcation diagram is identical to the one presented in [26], which validates our 2D simulations. The lengths in Fig. 6 (r_1 to r_4, as marked in Fig. 5(d)) are normalized with respect to the downstream channel width W. As in [26], the critical Reynolds number for the symmetry breaking Re_{sb} was found to be approximately 28.5, which is in good agreement also with the results in [22]. In fact, reference [22] considers $\lambda = 16$ and obtains a critical Reynolds number of 27.5, which is very close to what we get. At Re between 41 and 42, the third vortex appears. Thus, our results are in excellent agreement with other results independently published in fluids literature, and they show the basic features of Coanda effect, which we will continue to see in more complex 3D flows.
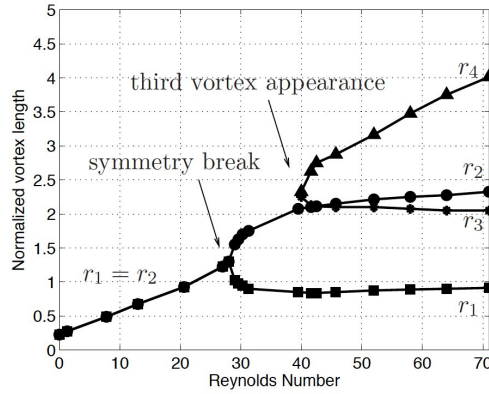
Figure 6: Bifurcation diagram for the geometry shown in Fig. 4(a) with expansion ratio $\lambda = 15.4$.

3.2. The 3D symmetric chamber

The stability analysis of the solution of the Navier-Stokes equations by direct flow simulation to characterize the asymptotic behavior of the solution can be extremely expensive in terms of computational time, especially in 3D. In [29], we developed Reduced Order Modeling techniques to reduce the demanding computational costs associated with the flow stability analysis in 3D geometries. In this section we use those techniques to show how the flow changes when the Reynolds number and the contraction-expansion channel geometry vary.

In 3D geometry reported in Fig. 4(b), the critical Reynolds number for the symmetry-breaking varies with the expansion ratio λ and the aspect ratio:

$$AR = \frac{H}{w},$$

9

as shown in [4, 5, 26, 29]. Here, we can think of H as the orifice length, and w the orifice height/width, and AR describing the orifice aspect ratio. This will be used as one of the parameters in Sec. 4 where 3D flows in the mock heart chamber are studied. When the expansion ratio λ of the channel is fixed and the aspect ratio decreases, the influence of the surrounding chamber walls becomes more important as 3D flow effects become more significant. Those are the contractions ("orifices") for which the 3D depth, described by H, is small relative to the contraction ("orifice") width w. For such flow regimes it was shown experimentally in [5, 26], and then theoretically in [17], that symmetry breaking and transition to wall hugging jets occurs at larger critical Reynolds numbers Re_{sb}. It is only for very large aspect ratios, i.e., for "orifices" that are long and narrow, that 3D flow though contraction-expansion channels resembles the corresponding 2D flow, as shown by the numerical studies in [40]. We will see later very similar behavior in the anatomically correct mock heart chamber and physiologic orifices.

To characterize the flow in 3D contaction-expansion channels, we introduce the normalized channel depth $\mathcal{H}$ defined by:

$$\mathcal{H} = \frac{H}{H + w} = \frac{AR}{AR + 1}.$$

Note that $\mathcal{H} = 1$ is the limiting case of infinite channel depth, which corresponds to the 2D configuration in Fig. 4(a). The Reynolds number for 3D flows defined in (13) can be written in terms of $\mathcal{H}$ as

$$Re_{3D} = \frac{\rho U w}{\mu} 2\mathcal{H}.$$

Let us consider $\lambda = 15.4$, as in the previous section. In order to show the sequence of events as the Reynolds number is increased when the aspect ratio is fixed, we set AR to 1.6398 which corresponds to $\mathcal{H} = 0.6210$. In Fig. 7, we display the streamlines on the vertical mid-plane for different values of the Reynolds number Re_{3D}. At $Re_{3D} = 0.01$, the 3D flow looks similar to the 2D flow (compare Fig. 7(a) with Fig. 5(a)) but it features smaller Moffatt eddies. As the Reynolds number increases, "lip vortices" form, as shown in Fig. 7(b). This is in agreement with the observations in [26] and references therein. The size of the lip vortices increases as Re_{3D} increases and once they reach the corner, the vortices continue to grow in the downstream direction. See Fig. 7(c), and (d). By convention, once they expand in the downstream direction they are called "corner vortices". Notice that the flow downstream of the expansion is symmetric up to $Re_{3D} = 76.8$, while asymmetries in 2D (i.e., for $\mathcal{H} = 1$) arise around $Re_{2D} = 28.5$.

Keeping the expansion ratio fixed to $\lambda = 15.4$, we consider now different values of $\mathcal{H}$. Fig. 8, 9, and 10 show the streamlines for the flow associated to $\mathcal{H} = 0.2085$, $\mathcal{H} = 0.6210$, and $\mathcal{H} = 0.9517$ for a small value, a medium value, and a large value of $Re_{3D} \in [0.01, 90]$. In particular, compare the solutions for $Re_{3D} = 90$ (leftmost panel in Fig. 8, 9, and 10). They clearly show that at low values of $\mathcal{H}$ the symmetry breaking bifurcation is pushed to higher values of Re_{3D} due the vertical walls. The strong three-dimensional effects appearing for low aspect ratios inhibit the wall-hugging effect observed in geometries with high aspect ratios at the same Reynolds number.

Based on the results presented in Sec. 3.1 and 3.2, we conclude that eccentric mitral regurgitant jets are produced by long (large $\mathcal{H}$) and narrow (large λ) orifices, and for larger Reynolds numbers. Our hypothesis is that mathematical Coanda effect occurs in mitral valves in which the leakage, i.e., regurgitation, occurs along a large section of the coaptation zone, rather than at an isolated point, leading to a possibly significant regurgitant volume.

10

(a) $Re_{3D} = 0.01$

(b) $Re_{3D} = 27.8$
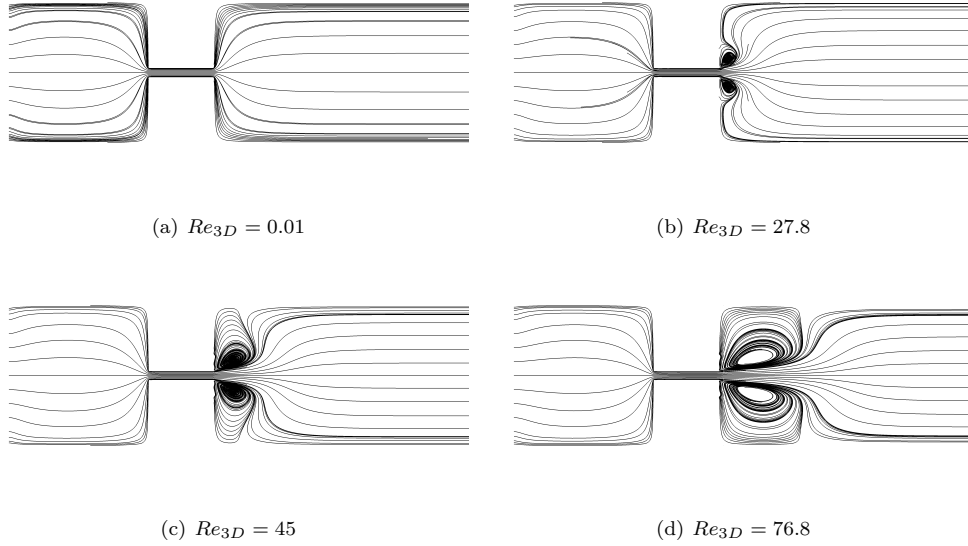
(c) $Re_{3D} = 45$

(d) $Re_{3D} = 76.8$

Figure 7: 3D contraction-expansion channel for $\lambda = 15.4$ and $\mathcal{H} = 0.6210$: streamlines on the vertical mid-plane (see figure 4(b)) for (a) $Re_{3D} = 0.01$, (b) $Re_{3D} = 27.8$, (c) $Re_{3D} = 45$, and (d) $Re_{3D} = 76.8$.
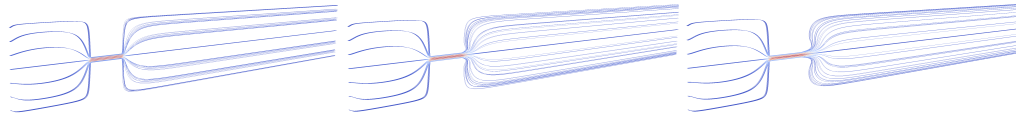
Figure 8: 3D contraction-expansion channel for $\lambda = 15.4$ and $\mathcal{H} = 0.2085$: streamlines for $Re_{3D} = 0.01$ (left), $Re_{3D} = 23$ (center), and $Re_{3D} = 90$ (right). The figure shows vertical mid-plane cut.
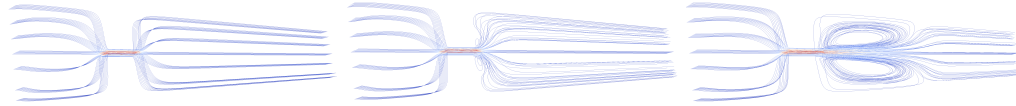
Figure 9: 3D contraction-expansion channel for $\lambda = 15.4$ and $\mathcal{H} = 0.6210$: streamlines for $Re_{3D} = 0.01$ (left), (b) $Re_{3D} = 13$ (center), and $Re_{3D} = 90$ (right). The figure shows vertical mid-plane cut.

Figure 10: 3D contraction-expansion channel for $\lambda = 15.4$ and $\mathcal{H} = 0.9517$: streamlines for $Re_{3D} = 4.5$ (left), $Re_{3D} = 27$ (center), and $Re_{3D} = 90$ (right). The figure shows vertical mid-plane cut.

11

4. 3D simulation of flow in mock heart chamber with physiological orifices

One of the goals of this study is to understand the details of complex flow conditions associated with eccentric regurgitant jets in the physiologically relevant scenarios, and understand how they may influence the echocardiographic assessment of severity of mitral valve regurgitation. For this
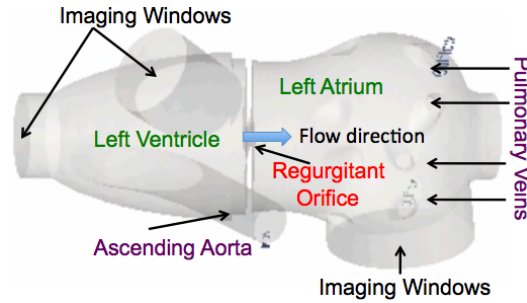
Figure 11: Geometry of the mock heart imaging chamber.

purpose, we use the flow results in the 2D and 3D symmetric contraction-expansion chambers, discussed above, as a motivation to understand the flow propertiescs through a physiologically relevant orifice in an anatomically correct heart chamber, shown earlier in Fig. 3, produced at the Methodist DeBakey Heart and Vascular Institute [15]. The mock chamber consists of a mock left ventricle and left atrium, which are connected via an orifice mimicking a regurgitant mitral valve. The interior of the chamber is shown in Fig. 11. The chamber was connected to a pulsatile flow loop generating realistic flow conditions, i.e., realistic trans-orifice pressure gradients during systole when mitral valve regurgitation is clinically significant. This means, in particular, that the generated flow travels backward from the left ventricle to the left atrium, which in the flow loop needs to be driven by the inlet data located in the left ventricle, and outlet data in the left atrium. The role of the inlet in our experiments is played by the mock ascending aorta connected to the left ventricle, see Fig. 11, and the role of the outlet, located in the left atrium, is played by the four mock pulmonary veins, as shown in Fig. 11. Since eccentric regurgitant jets that are associated with under-estimation of regurgitant volume typically occur in prolapsed mitral valves, we manufactured orifices that mimic those. A sketch of a prolapsed valve is shown in Fig. 12. Three

Figure 12: Sketch of a prolapsed mitral valve.

prolapsed orifices with different aspect ratios were manufactured using a 3D printer. See Fig. 13. The orifices are all rectangularly shaped, with the height equal to 1mm and widths equal to 10mm,

(a) Orifice 1:10   (b) Orifice 1:3.33   (c) Orifice 1:2.5
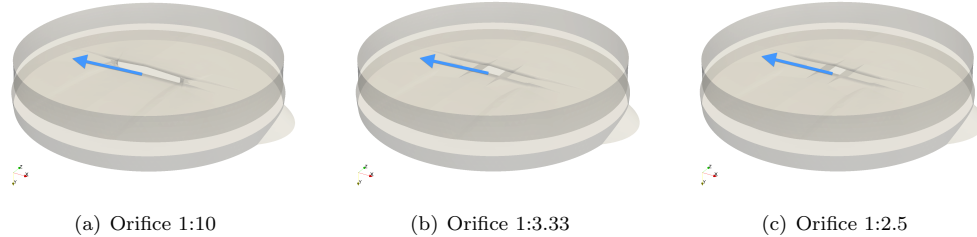
Figure 13: Orifices with three different aspect ratios. The arrow shows flow direction.

3.33mm and 2.5mm. They will be referred to as orifices with the aspect ratio 1:10, 1:3.33, and 1:2.5.

The flow in the mock heart chamber was simulated computationally, and the results of the simulations were compared with the echocardiographic image of regurgitant flow, and with *in vivo* trans-orifice pressure data. Since echocardiography does not provide detailed and precise information about flow, computer simulations were used to analyze point-wise velocity and flow conditions associated with regurgitant flows in the mock left atrium as two medically relevant flow parameters are varied: the regurgitant volume and regurgitant orifice size. They are related to two mathematically relevant, non-dimensional parameters: the Reynolds number and orifice aspect ratio. These two sets of parameters can be depicted in the same "bifurcation diagram", shown in Fig. 19, discussed in Sec. 4.2. Our findings are presented below.

4.1. Details of numerical strategy and validation

As mentioned above, the computational domain consists of mock left ventricle and mock left atrium connected by an orifice that mimics a leaky prolapsed mitral valve, see Fig. 13. The "gap" between two fixed "leaflets", i.e., the orifice, has a rectangular shape.

The mock chamber is discretized in space using a mesh of tetrahedra. We generated unstructured (non-uniform) meshes in order to capture the fine flow structures in different parts of the domain. In particular, the mesh gets finer near the orifice to resolve the details of the flow field. Meshes with different level of refinement were tested to guarantee that the simulation is mesh independent. In Table 1, we report the details of the meshes used for the simulations in Fig. 19. The name of the mesh refers to the simulation number and the level of refinement. Fig. 14 shows mesh Sim3.fine together with the dimensions of the heart chamber.

Fluid enters the computational domain through one inlet, which represents the ascending aorta, and it leaves the computational domain through four separate outlets, which represent the pulmonary veins. A flow rate was prescribed at the inlet (obtained from experimental measurements) and normal stress at the outlet. The results that we present below for validation purposes were obtained with the inlet flow rate data shown in Fig. 15(a) and with the stress-free outlet boundary condition. We imposed a time dependent parabolic velocity profile at the inlet producing the flow rate in Fig. 15(a). The rectangular orifice with 1:10 aspect ratio, shown in Fig. 13(a), was used in the validation simulations. The regurgitant volume associated to this flow rate data is 31 ml per beat (mild-to-moderate MR). On the rest of the domain, a non-slip boundary condition is enforced. This validation test corresponds to Case 3 in Fig. 19.

The density and the viscosity of the fluid are $\rho = 1$ g/cm^3 and $\mu = 0.035$ poise, respectively. The peak velocity magnitude averaged over the orifice section is around 554 cm/s and the hydraulic

Table 1: Meshes used for the simulations in Fig. 19. The name of the mesh refers to the simulation number and the level of refinement. The average mesh size is in cm.

Mesh Name	Number of Element	Average Mesh Size	Velocity DoF / Pressure DoF
Sim1.medium	2.05×10^6	0.184	8.73×10^6 / 0.38×10^6
Sim1.fine	2.26×10^6	0.168	9.54×10^6 / 0.41×10^6
Sim2.medium	2.02×10^6	0.183	8.55×10^6 / 0.37×10^6
Sim2.fine	2.39×10^6	0.155	9.98×10^6 / 0.43×10^6
Sim3.medium	1.81×10^6	0.185	7.84×10^6 / 0.34×10^6
Sim3.fine	2.81×10^6	0.142	11.8×10^6 / 0.52×10^6
Sim4.medium	2.01×10^6	0.183	8.49×10^6 / 0.37×10^6
Sim5.fine	5.41×10^6	0.135	22.56×10^6 / 0.99×10^6
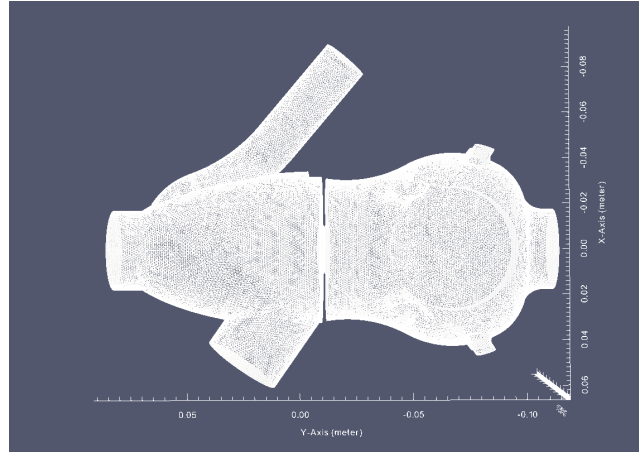
Figure 14: Mesh Sim3.fine with the dimensions of the mock heart chamber.

(a) Flow rate

(b) Transorifice pressure gradient
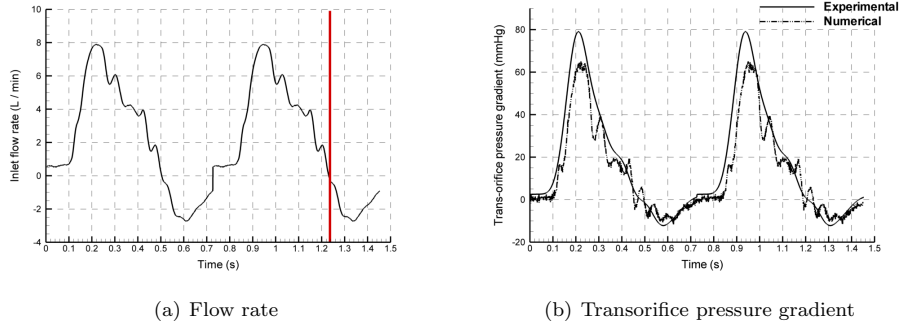
Figure 15: Experimentally measured hemodynamic conditions: (a) flow rate (L/min) and (b) pressure difference across the orifice ($mmHg$).

diameter of the orifice is 0.18 cm. Plugging these values into (5), we get a Reynolds number of around 2850. The time step that was used for the simulation with this Reynolds number was $\Delta t = 0.0002$. All the computational results presented in the rest of this section refer to mesh Sim3.fine (see Table 1).

The computational simulations were carried out by using the computing resources from Center for Advanced Computing and Data Systems (CACDS) at the University of Houston and Texas Advanced Computing Center (TACC) at the University of Texas at Austin. The Maxwell cluster at CACDS is a 3712-core cluster and each node has 64 GB memory (16 cores for each node and 4 GB memory for each node). The simulations presented here used 16 cores for each node with a total of 256 cores. At TACC we used the Stampede cluster. Each node has two Xeon E5-2680 processors and one Intel Xeon Phi SE10P Coprocessor. The simulations presented here used a total of 800 cores with 2 GB for each core.

We ran our computer simulations with the given, i.e., measured, inlet and outlet data, as specified above, and recorded the trans-orifice pressure gradient obtained from our computer simulations. The trans-orifice pressure gradient was then measured in the mock heart chamber using pressure transducers, and compared with our computer simulation results. Fig. 15(b) shows the comparison between the two, showing excellent agreement.
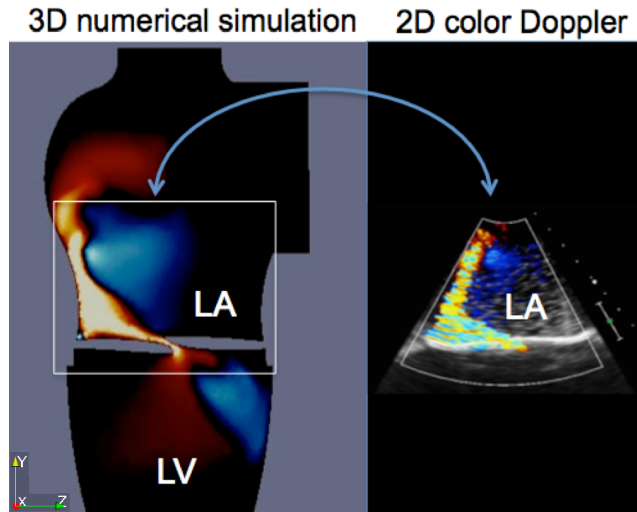
Figure 16: (a) Eccentric regurgitant jet. Left: A slice through the 3D mock heart chamber of the numerically computed y-component of the velocity in the yz-plane at time $t = 1.24$ s. Right: A 2D Doppler echocardiographic image of the regurgitant jet in the mock heart chamber at $t = 1.24$ s. The two sub-figures have the same color scale: -50 cm/s to 50 cm/s. Conic distortion in the right panel occurs due to the use of convex array transducer.

To compare the numerically calculated regurgitant jet with the one measured using 2D color Doppler, we plot the computed regurgitant jet velocity in the direction aligned with the direction of the ultrasound, i.e., we plot the y-component of the fluid velocity in the yz-plane, as shown in Fig. 16 (left). A comparison between the two is shown in Fig. 16. In comparing the results shown in Fig. 16 left and right, one needs to take into account that the Doppler image is obtained by a convex array transducer. Thus, the image looks wider with increasing depth (fan shape). The reason why convex arrays transducers are used instead of linear array transducers (which produce

rectangular images easy to look at) is that convex array transducers have lower frequencies and more penetration. This is a clear advantage in clinical examinations. By taking this information into account, we can conclude that the jet shape and wall hugging in both panels looks very close. Additionally, the range of velocities (in the y-direction) is the same in both figures, which is between -50 cm/s and 50 cm/s. Furthermore, notice how in both figures there is a dark blue region near the center of the mock left atrium indicating the flow direction away from the transducer, i.e., in the negative y-direction. This indicates the presence of a large vortex, as we shall see below.
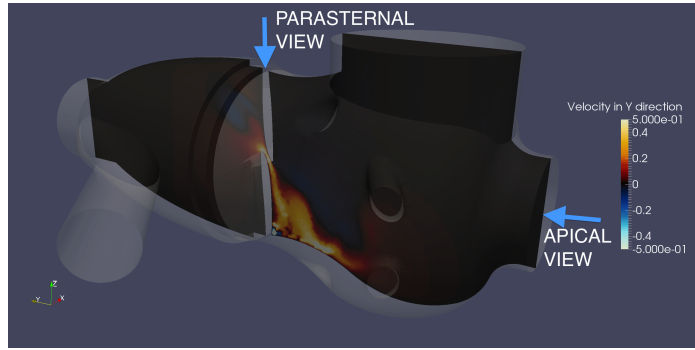
(a) y-component of the velocity
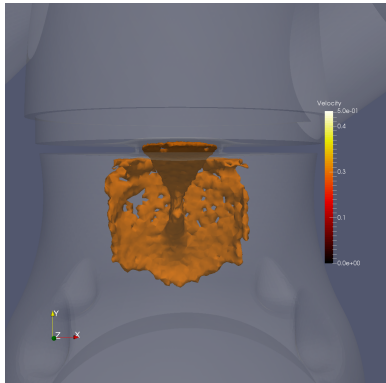
(b) Isovelocity Surface (Parasternal View)   (c) Isovelocity Surface (Apical View)
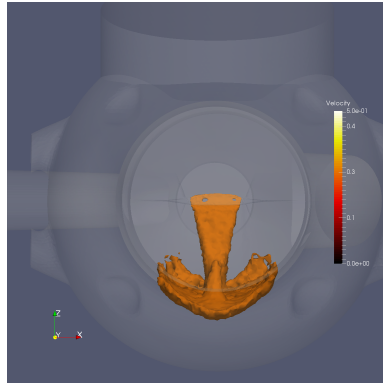
Figure 17: Views of the regurgitant jet at time $t = 1.24$ s: (a) y-component of the velocity in the yz-plane, with the color scale from -50 cm/s to 50 cm/s; (b) Parasternal View and (c) Apical View of the isovelocity surface corresponding to 30 cm/s.

A further inspection of the ultrasound Doppler image in Fig. 16 (right) shows that there is a region near the orifice plate that contains light blue color, indicating some backward flow. This light blue color is superimposed over the yellow and red flow regions, indicating positive flow. Indeed, we can observe the same behavior in the numerically simulated flow if we plot the 3D isovelocity surfaces, shown in Fig. 17. More precisely, panels (b) and (c) in Fig. 17 show that the Coanda jet hits the side wall of the atrial chamber and produces a splash with backward flow aligned with the walls of the chamber. Moreover, from Fig. 17(a) it appears that there is a small vortex shown in

blue at the corner where the orifice plate meets the atrial chamber wall. This corresponds to the small vortices on the left side of the Coanda jet in the 2D simulation of Coanda effect, shown in Fig. 5 (d).

Finally, as shown earlier in the stylized simulations of 2D and 3D Coanda effect, we expect to see a large vortex in the middle of the chamber that "pushes" the regurgitant jet toward the wall. Indeed, Fig. 18 (right) shows a 2D cut in the yz-plane of the velocity vector field inside the mock heart chamber indicating a large vortex pushing the regurgitant jet closer to the atrial wall. The short arrows in this figure indicate flow in the direction orthogonal to the yz-plane. Indeed, in
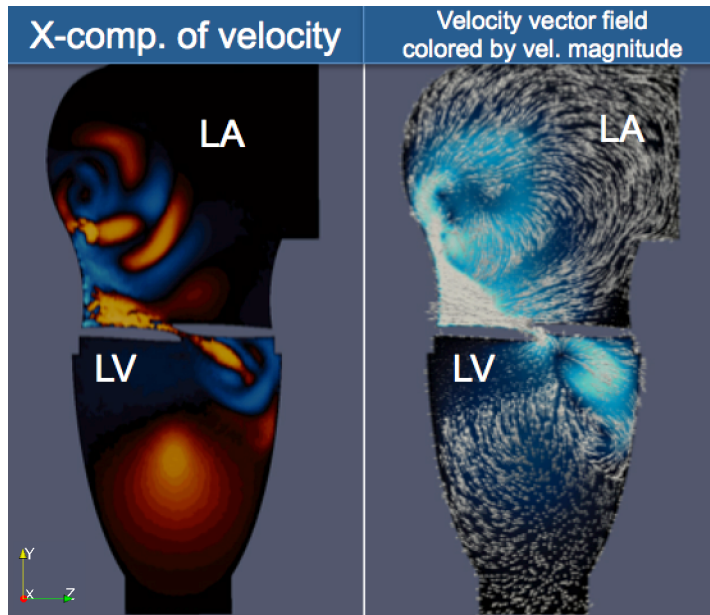
Figure 18: Regurgitant jet at time $t = 1.24$ s. Left: x-component of the velocity in the yz-plane. The red dot in LV shows the location of the inlet. Right: velocity vector field colored by the velocity magnitude.

Fig. 18 left we plot the x-component of the velocity, i.e., the component orthogonal to the yz-plane. Interestingly enough, we see vortex-shaped regions of red/yellow and blue flow, i.e., forward and backward flow moving toward and away from the viewer. This is a signature of a doughnut-shaped vortex roll. The velocity vector field colored by the magnitude of the velocity, shown in Fig. 18 right, shows a more clear depiction of the vortex roll located in the mock left atrium (LA). This is the first finding of a vortex roll associated with regurgitant Coanda jets in the left atrium. The role of vortex dynamics in the left ventricle has been studied by several authors, see e.g., [10, 28]. It has been postulated in [28] that maladapted intracardiac vortex dynamics might modulate the progressive remodeling of the left ventricle towards heart failure. The role of the vortex dynamics in the left atrium is, however, completely unexplored.

To gain a deeper understanding of the formation of Coanda jets, vortex rolls, and their influence on echocardiographic assessment of MR, we continue our study by analyzing different types of flows that occur as we vary two clinically relevant parameters: regurgitant volume and orifice size. They are related to two non-dimensional mathematically relevant parameters: the Reynolds number and

Table 2: Orifice size, regurgitant volume (RV), Reynolds number, mesh, and number of cores for every simulation under consideration.

Simulation	Orifice	RV (ml/beat)	Re	Mesh Name	CPUs (cores)
1	1:2.5	7.75	2850	Sim1.fine	800
2	1:3.33	10.3	2850	Sim2.fine	800
3	1:10	31	2850	Sim3.fine	800
4	1:10	10.3	950	Sim4.medium	256
5	1:3.33	31	8550	Sim5.fine	800

orifice aspect ratio, that describe the clinically interesting scenarios of regurgitant flow in the left atrium. We present our results next.

4.2. A 2-parameter study of 3D regurgitant flow

We present a 2-parameter study of 3D flow through "regurgitant" orifices. Two mathematically equivalent sets of parameters are going to be considered:

- The orifice aspect ratio, and

- Regurgitant volume

and the corresponding non-dimensional parameters:

- The orifice aspect ratio, and

- Reynolds number.

By increasing regurgitant volume with fixed orifice aspect ratio (orifice size), the Reynolds number increases.

As mentioned earlier, we consider 3 different orifices. They all have the same height: 1mm, while the widths are: 10mm, 3.33 mm, and 2.5 mm, resulting in three orifices with aspect ratios 1:10, 1:3.33, and 1:2.5. See Fig. 13. Furthermore, we varied the inflow velocity to obtain 3 different regurgitant volumes: 31 ml/beat, 10.3 ml/beat, and 7.75 ml/beat. Five simulations were performed: Case 1, Case 2, Case 3, Case 4, and Case 5. The corresponding parameters are reported in Fig. 19. Cases 1, 2, and 3, which sit on the diagonal in the graph in Fig. 19, all have the same Reynolds number: Re = 2850. Case 4, which is below the diagonal, has a smaller Reynolds number: Re=950, and Case 5, which is above the diagonal, has a larger Reynolds number: Re=8550. Detailed data associated with each simulation is reported in Table 2.

For each of the simulations in Table 2, we ran two complete systolic cycles and we compared the regurgitant jet at the time of peak flow rate during the second cycle ($t = 1.24$ s).

Detailed plots of the y-components of velocity for all 5 cases are shown in Fig. 20. Also, small images containing the y-components of velocity for each case are inserted in the parameter space diagram shown in Fig. 19. For better viewing the large plots in Fig. 20 are organized in the same order as they appear in Fig. 19.

The plots of the corresponding velocity vector fields superimposed over the velocity magnitude for each of the five Cases are shown in Figs. 21–25. There are several mathematically relevant

18
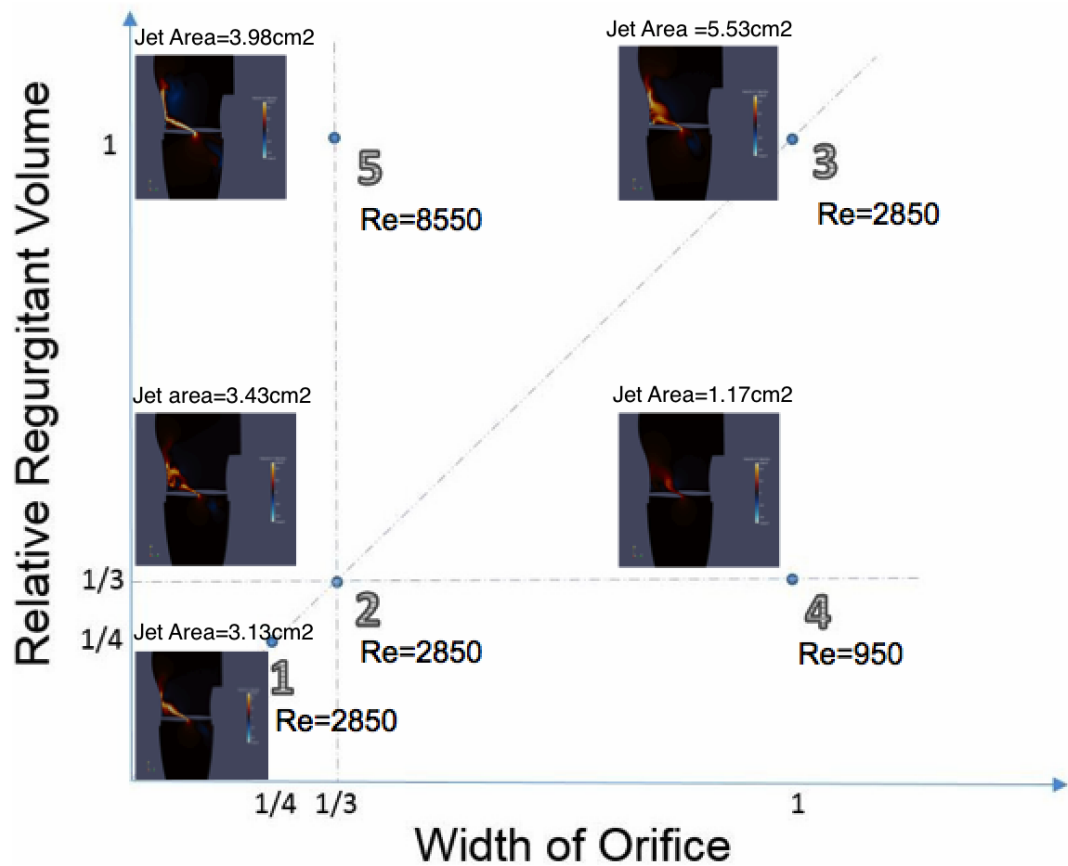
Figure 19: Parameter space showing five different simulations (Cases). The corresponding Reynolds number are: Case 1: Re=2850; Case 2: Re=2850; Case 3: Re=2850; Case 4: Re=950; Case 5: Re=8550. The vertical axis denotes regurgitant volume **relative** to RV=31 ml/beat. Relative RV of 1/3 corresponds to RV=31/3=10.3 ml/beat, and relative RV of 1/4 corresponds to RV=31/4=7.75 ml/beat. The horizontal axis correspond to the **relative** orifice width with respect to the orifice width of 10mm and aspect ratio 1:10. The numbers 1/4 and 1/3 correspond to the orifices if width 2.5 mm and 3.33 mm, respectively.
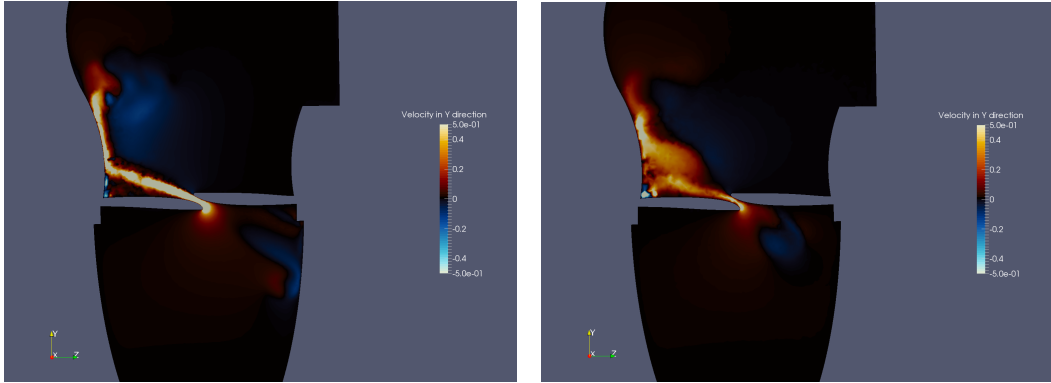
(a) <u>Case 5</u>: Orifice: 1:3.3; Reg. Vol.=31 ml/b; Re=8550 (b) <u>Case 3</u>: Orifice: 1:10; Reg. Vol.=31 ml/b; Re=2850
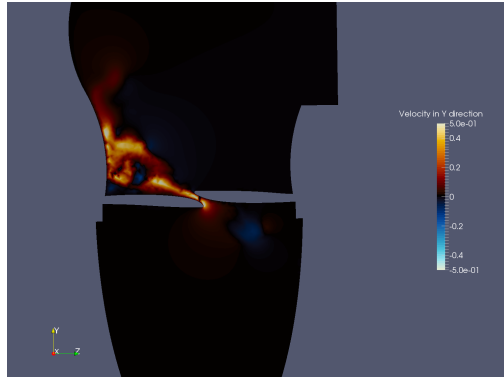
(c) <u>Case 2</u>: Orifice: 1:3.3; Reg. Vol.=10.3 ml/b; Re=2850
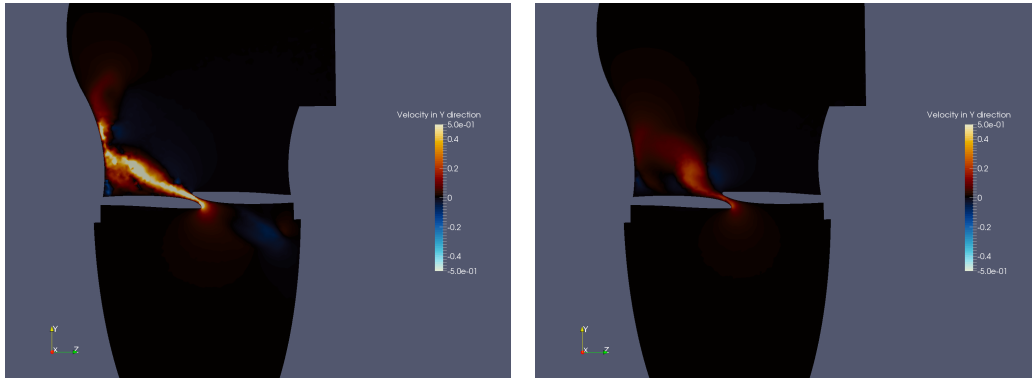
(d) <u>Case 1</u>: Orifice: 1:2.5; Reg. Vol.=7.76 ml/b; Re=2850 (e) <u>Case 4</u>: Orifice: 1:10; Reg. Vol.=10.3 ml/b; Re=950

Figure 20: Computed y-component of the velocity in the yz-plane at time $t = 1.24$ s for the five cases shown in Fig. 19. The sub-figures are displayed in the same order as in Fig. 19. The cases on the "diagonal" are Cases 1, 2, and 3, all with the same Re=2850 but increasing orifice aspect ratio. Below the diagonal is Case 4 with Re=950, and above the diagonal is Case 5 with Re=8550.
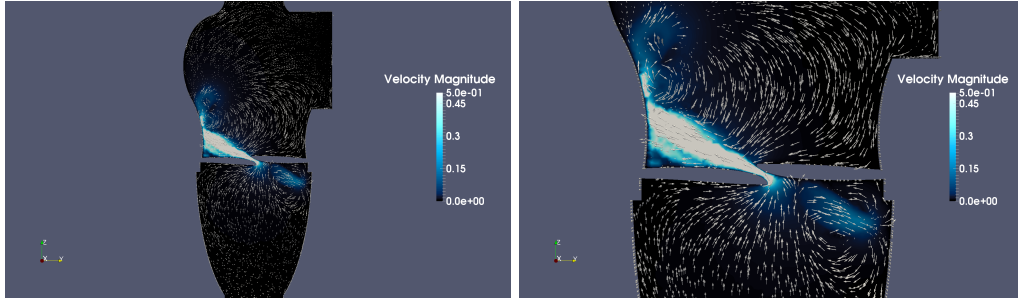
Figure 21: Case 1 (1/4,1/4) in Fig. 19. Left: 2D slice of 3D velocity vector field in mock heart chamber. Right: magnified view near the orifice. Velocity magnitude scale is saturated at 0.5 m/s for sharper identification of regurgitant jet and for better viewing of flow structures at smaller velocities.
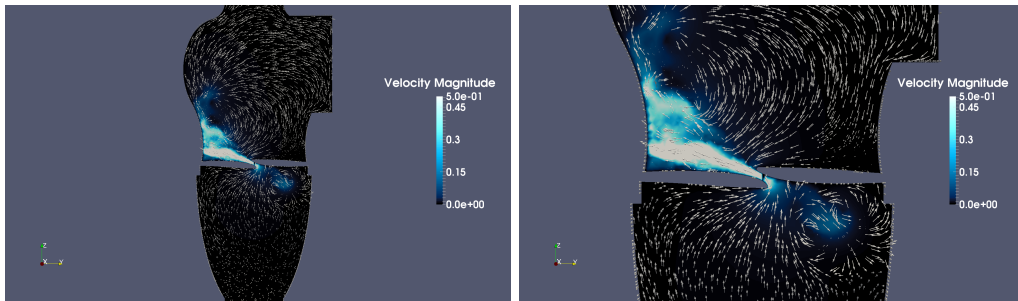
Figure 22: Case 2 (1/3,1/3) in Fig. 19. Left: 2D slice of 3D velocity vector field in mock heart chamber. Right: magnified view near the orifice. Velocity magnitude scale is saturated at 0.5 m/s for sharper identification of regurgitant jet and for better viewing of flow structures at smaller velocities.
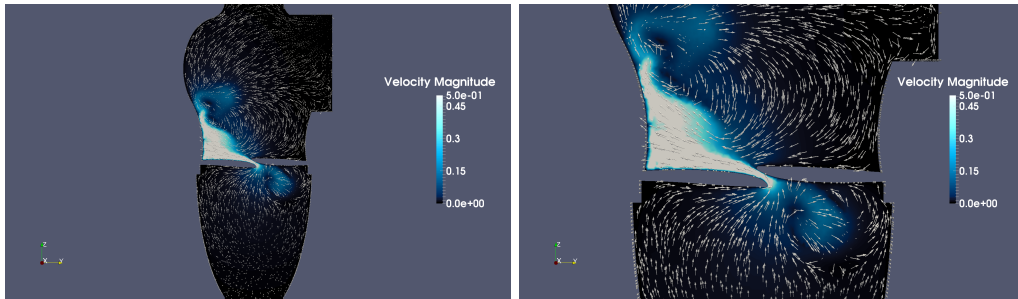
Figure 23: Case 3 (1,1) in Fig. 19. Left: 2D slice of 3D velocity vector field in mock heart chamber. Right: magnified view near the orifice. Velocity magnitude scale is saturated at 0.5 m/s for sharper identification of regurgitant jet and for better viewing of flow structures at smaller velocities.
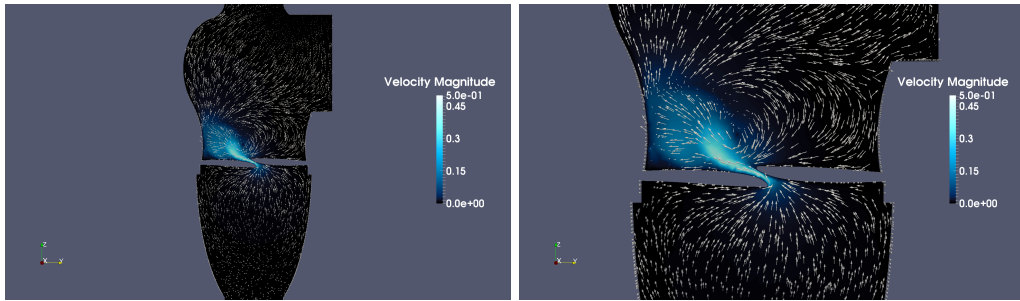
Figure 24: Case 4 (1,1/3) in Fig. 19. Left: 2D slice of 3D velocity vector field in mock heart chamber. Right: magnified view near the orifice. Velocity magnitude scale is saturated at 0.5 m/s for sharper identification of regurgitant jet and for better viewing of flow structures at smaller velocities.
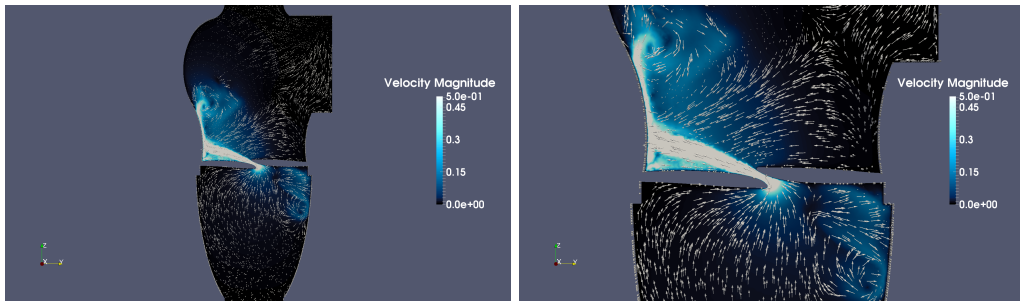
Figure 25: Case 5 (1/3,1) in Fig. 19. Left: 2D slice of 3D velocity vector field in mock heart chamber. Right: magnified view near the orifice. Velocity magnitude scale is saturated at 0.5 m/s for sharper identification of regurgitant jet and for better viewing of flow structures at smaller velocities.

and clinically relevant conclusions that can be obtained from these simulations. They are discusses below.

Mathematical flow bifurcation to Coanda effect. Based on the diagram shown in Fig. 19 and on the detailed regurgitant jet velocity plots in Fig. 20 and in Figs. 21–25 we can conclude several interesting mathematical properties of flow behavior.

Firstly, we focus on the diagonal in Figs. 19 and 20, i.e., Cases 1, 2, and 3. They all correspond to the same Reynolds number Re=2850, with an increasing orifice length as we move from Case 1 to 3. This corresponds to moving closer to the 2D flow for orifices with larger aspect ratio, which implies that for longer orifices we expect to see transition to the wall-hugging behavior, as shown in Fig. 5. Indeed, this is what is happening in the 3D mock heart chamber, however, we need to be careful to explain what do we mean by the "wall hugging behavior", or Coanda effect, in prolapsed orifices.

Coanda effect. Since all three orifices correspond to prolapsed orifice, i.e., the orifice itself is almost orthogonal to the orifice plate, we expect to see eccentric jets directed by the orifice to one side in all flow regimes. "Wall hugging" in this case corresponds to the jet closely hugging the *bottom leaflet* of the orifice. This is what was named Coanda effect when it was first observed in aerodynamics [39]. See Fig. 2. Instead of shooting away from the orifice plate sideways toward one of the walls of the atrial chamber, the jet "hugs" the bottom leaflet of the orifice plate. Thus, we will consider the bifurcation of flow to Coanda effect to occur when the jet through the prolapsed orifice is *attached* to the bottom orifice plate.

A close inspection of the three cases corresponding to the same Re=2850 indicates that the first time we observe hugging by the regurgitant jet of the leaflet sitting on the left side of the orifice, i.e., the bottom leaflet, is in Case 3, which corresponds to the longest orifice, i.e., the orifice with aspect ratio 1:10. A zoom into the region close to the orifice confirming this behavior is shown in Fig. 23. Therefore, we conclude that bifurcation to Coanda effect, i.e., hugging of the leaflet by the regurgitant jet, occurs in the 3D mock heart chamber for orifices with larger aspect ratios. This is consistent with the stylized 2D and 3D findings reported in Secs. 3.1 and 3.2.

Next, we observe that with the increase in Reynolds number, for small aspect ratios, see e.g. Case 5, there is no hugging of the left leaflet. Similarly, if the Reynolds number is small, even with the large orifice aspect ratio, as in Case 4, there is no significant hugging of the left leaflet. Therefore, we conclude that bifurcation to Coanda effect occurs in the mock heart chamber when both the Reynolds number and the aspect ratio of the orifice are large. Therefore, we postulate that the bifurcation diagram to Coanda effect looks like the diagram shown in Fig. 26.

In the remainder of this section we further investigate the influence of the orifice aspect ratio and the Reynolds number on general flow properties in the 3D mock heart chamber. We first study the impact of orifice aspect ratio and then the Reynolds number.

Aspect Ratio. Recall that 2D and 3D simulations indicate that the longer the orifice relative to its width, the more 2D, rather than 3D flow features will be present. Thus, for shorter offices, namely for the orifices in Cases 1, 2, and 5, we expect to see more pronounced 3D flow features. Indeed, if we look at Figs. 21, 22, and 25 we see large regions in the atrial chamber that have very short white arrows. This means that the flow is directed toward or away from the viewer, i.e., in the direction orthogonal to the yz-plane. This is particularly obvious in Figs. 21 and 25 that correspond to Re=2850 and Re=8550, respectively.

Thus, we conclude that as we change the aspect ratio of the orifice, the smaller the aspect ratio, the more pronounced are the 3D flow features.

Reynolds Number. Now we focus on the flow behavior as the Reynolds number increases. In the diagram shown in Fig. 19 the increase in the Reynolds number is captured by moving transversely
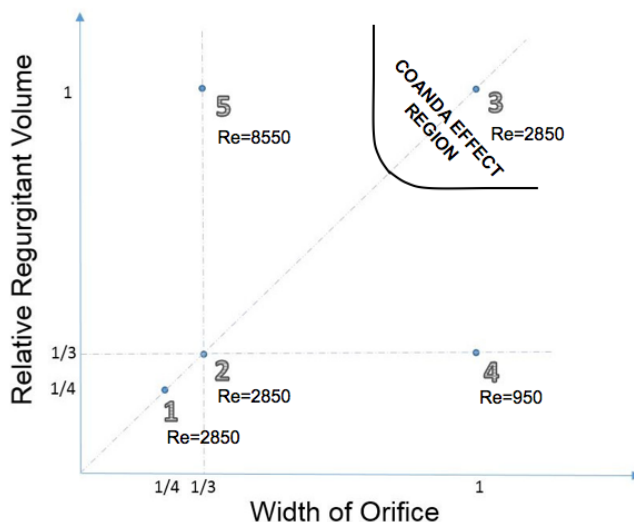
Figure 26: Hypothesized bifurcation diagram showing when the transition to Coanda effect occurs in the 3D mock heart chamber. The diagram suggests that large Reynolds numbers and orifice ratios are needed to observe a true wall (leaflet) hugging effect.

across the diagonal from bottom right to top left. Thus, we focus on Cases 4, 3, and 5. An inspection of Figs. 24, 23, and 25 corresponding to these three cases shows that the center of the vortex that is formed near the end of the regurgitant jet moves closer to the atrium wall, and the jet becomes longer as we move from Case 4 to Case 3 and then Case 5. Thus, an increase in the Reynolds number gives rise to longer, stronger jets with a larger vortex whose center is located higher in the chamber. We notice that in Case 5, which also features an orifice with small aspect ratio, there are strong 3D effects that additionally influence the flow.

> **In summary:** the increase in orifice aspect ratio makes the flow closer to two-dimensional at least locally, near the orifice, while the increase in the Reynolds number makes the jet stronger, longer, and pushes the center of the large interior vortex higher up and closer to the atrium wall. Coanda effect, i.e., the hugging of the bottom leaflet of the orifice plate, occurs for large orifice ratios and larger Reynolds numbers.

Clinical Relevance.

The primary clinical tool to estimate severity of mitral valve regurgitation (MR) is echocardiography. Since surgery is recommended for severe mitral regurgitation, accurate estimation of MR is imperative. Color Doppler is commonly used to screen for MR. The color Doppler imaging depicts spatial distribution of velocities within the imaging plane. Despite published guidelines recommending otherwise, in many busy clinical settings the color Doppler jet area is often still used as the first tool to estimate the severity of MR [12, 42]. The color Doppler jet area technique is based on estimating, or calculating the jet area that is seen on a 2D color Doppler image. Central jets typically appear larger. In medical literature this is typically associated with red blood cell entrainment by the flow vortices [12]. Eccentric jets can entrain particles, but mostly only on one side, i.e., on the side of the jet adjacent to the center of the left atrium. Figs. 27 and 28 show how
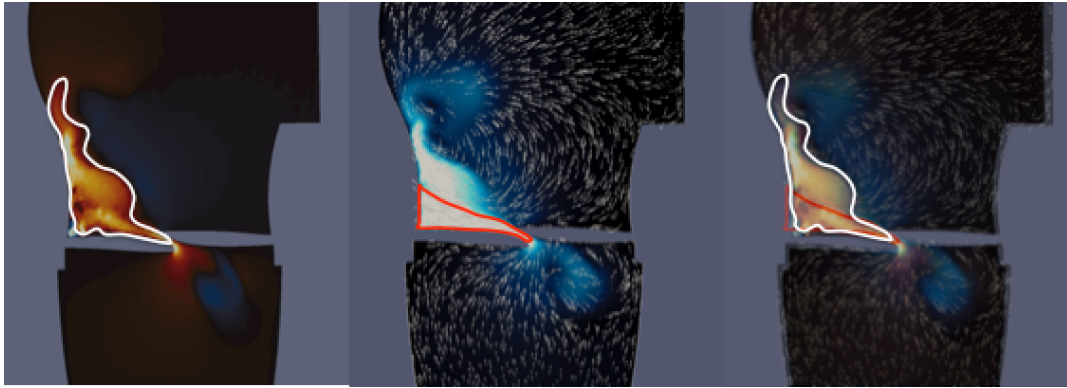
Figure 27: Case 3: RV = 31 ml/beat, Orifice aspect ratio 1:10, Re=2850. Left: Jet area as seen by 2D color Doppler. Middle: Actual jet area, which excludes the portion of the entrained particles by the jet, belonging the large vortex located on the right of the jet. Right: Superposition of the two.
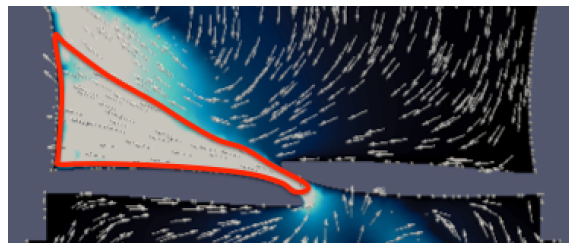
Figure 28: Case 3: RV = 31 ml/beat, Orifice aspect ratio 1:10, Re=2850. A magnified view of the jet area showing recirculating flow from the large vortex adjacent to the jet, which contaminates estimation of the size of the jet area.

a vortex located near the center of the left atrium chamber enlarges the observable jet area of the Coanda jet in Case 3, discussed above. Fig. 27 shows the jet area as it would be estimated by an imaging observer (left panel), the actual jet area (middle panel), and the difference between the two (right panel).
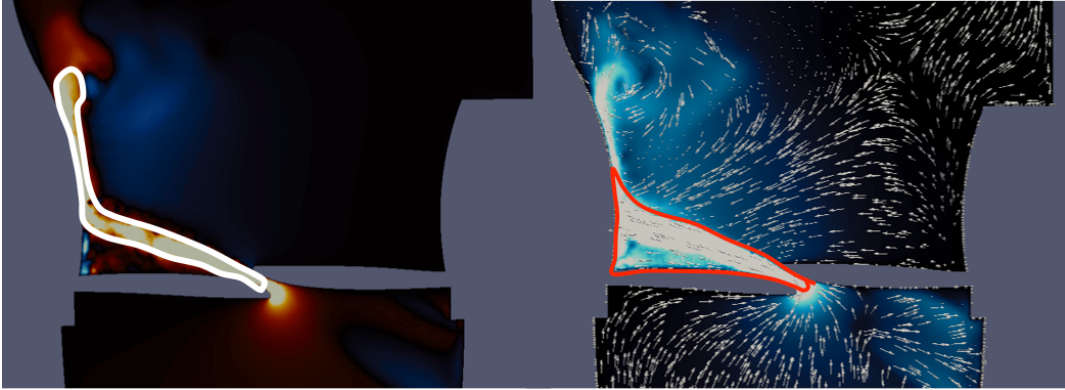
Figure 29: Case 5: RV = 31 ml/beat, Orifice aspect ratio 1:3.3, Re=8550. Left: Jet area as seen by 2D color Doppler. Right: Actual jet area.
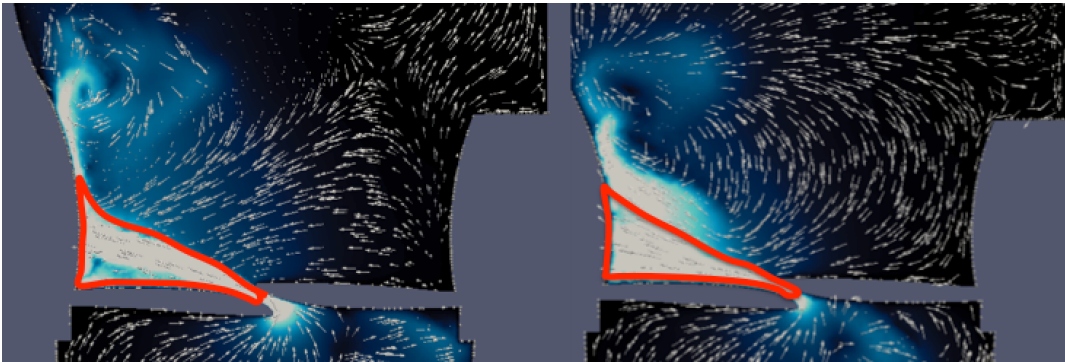
Figure 30: Comparison in actual jet area size between Case5 (left) and Case 3 (right).

In this particular case we see that there is a large difference between the two. A magnified view of the jet, shown in Fig. 28, shows the reason why the jet area looks bigger: the adjacent vortex that pushes the jet closer to the atrium wall contains a region with the recirculating vortex flow that has the same velocity as the original jet, making the appearance of the jet larger than it actually is. Notice that this case corresponds to a large orifice aspect ratio (OAR: 1:10), in which case the apical view of the flow picks up the 2D flow features of Coanda effect associated with larger orifice aspect ratios and larger Reynold numbers.

Thus, the presence of the large vortex located near the center of the left atrium recirculates the flow in that area, and makes the regurgitant jet appear larger than it actually is, but only on that one side.

26

For comparison, we also show the jet area associated with the flow in Case 5, discussed above. The panel on the left in Fig. 28 shows the jet area as it would be estimated by an imaging observer, while the panel on the right in the same figure shows the actual jet area. We report below in Fig. 31 and in the diagram shown in Fig. 19 the observable jet area size: for Case 5, the estimated jet area as seen in the simulations shown in Figs. 19 and 31 is 3.98 cm^2, and the jet area for Case 3 is 5.53 cm^2. We see that the two jet areas are significantly different even though they are associated with the same RV.

We remark that in Case 5, shown in Fig. 29 the reasons for why the jet area appears smaller are the 3D flow effects which are much more pronounced in orifices with small aspect ratio, as discussed above. As a consequence, the vortices with strong flows in the x-direction, i.e., orthogonal to the yz-plane corresponding to the apical view in the 2D Doppler image, have a significant presence in the left atrium chamber, which cannot be seen in the 2D color Doppler image. In particular, in Fig. 29 we see that small vortices even under the jet appear, making the jet area appear smaller than it actually is.

In Fig. 30 we show a comparison in *actual* jet area size between Cases 3 and 5. We observe that the actual jet areas are quite comparable.

Based on the result presented in this manuscript, the following clinically relevant conclusions can be made:

1. Regurgitant jets associated with prolapsed mitral valves can be classified into two categories: **deflected jets** and **Coanda jets**. Deflected jets follow the direction of flow determined by the prolapsed orifice, while Coanda jets exhibit strong wall-hugging behavior from the moment they exit the orifice and enter the left atrium.

2. Coanda jets typically occur for larger orifice aspect ratios and larger Reynolds numbers, which are associated with larger regurgitant volumes.

3. Using a single plane 2D color Doppler jet area size methodology to estimate the severity of mitral regurgitation is not a reliable tool for estimation of regurgitant volume.

4. Regurgitant jets passing though prolapsed orifices with small aspect ratio exhibiting large regurgitant volumes, such as e.g., Case 5 discussed above, have significant 3D flow features that cannot be captured by single plane 2D color Doppler screening. Such jets are more likely to be under-estimated in severity of mitral regurgitation.

5. **Vortex rolls** appear in the left atrium for regurgitant jets passing through orifices with larger Reynolds numbers. The smaller the orifice aspect ratio, the larger the 3D vortex roll effects. This is the first time vortex rolls have been associated with regurgitant jets in the left atrium. It has been postulated in [28] that maladapted intracardiac vortex dynamics might modulate the progressive remodeling of the left ventricle towards heart failure. The role of regurgitant vortex dynamics in the left atrium on LA remodeling is, however, completely unexplored.

5. Conclusions

This work presents a comprehensive analysis of regurgitant mitral valve flows in the the left atrium. A two-parameter study of flow showing transition to eccentric, wall-hugging Coanda jets was performed, explaining the role of orifice aspect ratio and regurgitant volume in the formation of Coanda jets. A bifurcation diagram showing transition to eccentric Coanda jets is postulated, showing that the true hugging of the mitral valve leaflet in eccentric jets occurs for orifices with a large aspect ratio, i.e., long and narrow orifices, and for larger regurgitant volumes. For the first
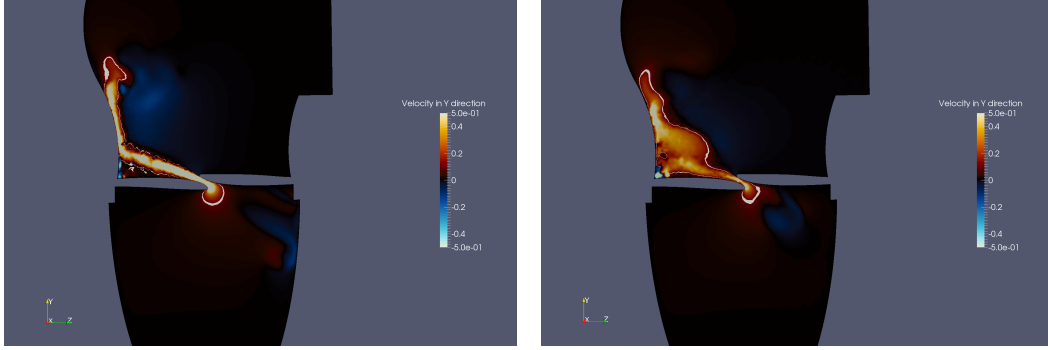
(a) <u>Case 5</u>: Jet Area: 3.98 cm^2 RV=31 ml/b OAR: 1:3.3   (b) <u>Case 3</u>: Jet Area: 5.53 cm^2 RV=31 ml/b OAR: 1:10
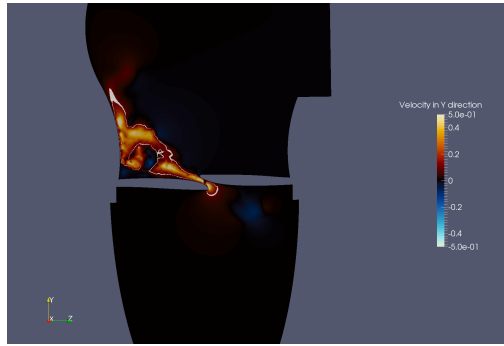
(c) <u>Case 2</u>: Jet Area: 3.43 cm^2 RV=10.3 ml/b; OAR: 1:3.3
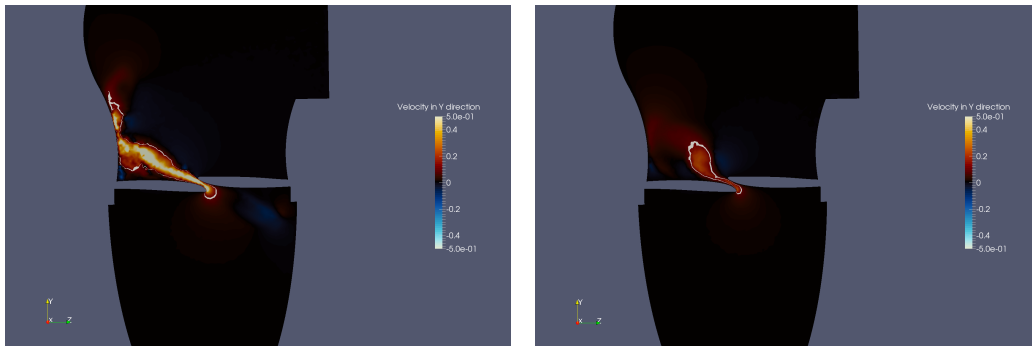
(d) <u>Case 1</u>: Jet Area: 3.13 cm^2 RV=7.76 ml/b OAR:1:2.5   (e) <u>Case 4</u>: Jet Area: 1.17 cm^2 RV=10.3 ml/b OAR:1:10

Figure 31: Computed **jet area** for the five cases shown in Fig. 19. RV denotes Regurgitant Volume, and OAR denotes Orifice Aspect Ratio. The sub-figures are displayed in the same order as in Fig. 19. The cases on the "diagonal" are Cases 1, 2, and 3, all with the same Re=2850 but increasing orifice aspect ratio. Below the diagonal is Case 4 with Re=950, and above the diagonal is Case 5 with Re=8550.

time vortex rolls have been detected in the left atrium regurgitant flow, and their role on underestimation of regurgitant volume using 2D color Doppler echocardiography explained. While the role of vortices in the left *ventricle* has been studied in the past [10, 28], the presence of vortex rolls in the left atrium during regurgitation is new. In the left ventricle, the work reported in [28] postulates that there is a connection between the maladapted intracardiac vortex dynamics and the progressive remodeling of the left ventricle. It would be interesting to see if the presence of vortex rolls in the left atrium during regurgitation, discussed in our work, is associated with the known LA remodeling in patients with severe MR. Perhaps one of the goals of a successful mitral valve repair would be to minimize (or optimize) LA vortex dynamics that may speed up reverse remodeling of LA, as reported in [21]. Thus, we have introduced a new concept in clinical imaging which emphasizes that the *quality* and not only the *quantity* of regurgitant flow matters in the assessment of severity of mitral valve regurgitation.

Acknowledgements

References

[1] LifeV - A parallel Finite Element library. www.lifev.org.

[2] L. Bertagna, A. Quaini, and A. Veneziani. Deconvolution-based nonlinear filtering for incompressible flows at moderately large reynolds numbers. *International Journal for Numerical Methods in Fluids*, 81(8):463–488, 2016.

[3] K. Chao, V.A. Moises, R. Shandas, T. Elkadi, D.J. Sahn, and R. Weintraub. Influence of the Coanda effect on color Doppler jet area and color encoding. *Circulation*, 85:333–341, 1992.

[4] W. Cherdron, F. Durst, and J.H. Whitelaw. Asymmetric flows and instabilities in symmetric ducts with sudden expansions. *J. Fluid Mech.*, 84:13–31, 1978.

[5] T.P. Chiang, Tony W.H. Sheu, and S.K. Wang. Side wall effects on the structure of laminar flow over a plane-symmetric sudden expansion. *Computers & Fluids*, 29(5):467 – 492, 2000.

[6] D. Drikakis. Bifurcation phenomena in incompressible sudden expansion flows. *Phys. Fluids*, 9(1):76–87, 1997.

[7] F. Durst, A. Melling, and J.H. Whitelaw. Low Reynolds number flow over a plane symmetric sudden expansion. *J. Fluid Mech.*, 64:111–128, 1974.

[8] A. Gauthier, F. Saleri, and A. Veneziani. A Fast Preconditioner for the Incompressible Navier Stokes Equations. *Computing and Visualization in Science*, 6(2):105–112, 2004.

[9] P. Gervasio, F. Saleri, and A. Veneziani. Algebraic fractional-step schemes with spectral methods for the incompressible Navier-Stokes equations. *J. Comp. Phys*, 214(1):347–365, 2006.

[10] M. Gharib, E. Rambod, A. Kheradvar, D.J. Sahn, and J.O. Dabiri. Optimal vortex formation as an index of cardiac health. *Proceedings of the National Academy of Sciences of the US*, 103(16):63056308, 2006.

[11] C. Ginghina. The Coanda effect in cardiology. *J. Cardiovasc. Med.*, 8:411–413, 2007.

[12] P.A. Grayburn, N.J. Weissman, and J.L. Zamorano. Quantitation of mitral regurgitation. *Circulation*, 126(16):2005–2017, 2012.

[13] P. Hariharan, M. Giarra, V. Reddy, S.W. Day, K.B. Manning, S. Deutsch, S.F.C. Stewart, M.R. Myers, M.R. Berman, G.W. Burgreen, E.G. Paterson, and R.A. Malinauskas. Multilaboratory Particle Image Velocimetry analysis of the FDA benchmark nozzle model to support validation of Computational Fluid Dynamcis simulations. *J. Biomech. Engrg.*, 133:041002, 2011.

[14] T. Hawa and Z. Rusak. The dynamics of a laminar flow in a symmetric channel with a sudden expansion. *J. Fluid Mech.*, 436:283–320, 2001.

[15] M.S. Jackson, S.R. Igo, T.E. Lindsey, D. Maragiannis, K.E. Chin, K. Autry, D.J. Shah, P. Valsecchi, W.B. Kline, and S.H. Little. Development of a multi-modality compatible flow loop system for the functional assessment of mitral valve prostheses. *Cardiovascular Engineering and Technology*, 5(1):13–44, 2014.

[16] P. Lancellotti, Ch. Tribouilloy, A. Hagendorff, B.A. Popescu, T. Edvardsen, L. A. Pierard, L. Badano, and J. L. Zamorano. Recommendations for the echocardiographic assessment of native valvular regurgitation: an executive summary from the European Association of Cardiovascular Imaging. *European Heart Journal-Cardiovascular Imaging*, 14:611–644, 2013.

[17] Eric Lauga, Abraham D. Stroock, and Howard A. Stone. Three-dimensional flows in slowly varying planar geometries. *Physics of Fluids*, 16(8):3051–3062, 2004.

[18] S. H. Little, S.R. Igo, M. McCulloch, C. J. Hartley, Y. Nosé, and W. A. Zoghbi. Three-dimensional ultrasound imaging model of mitral valve regurgitation: design and evaluation. *Ultrasound in Med. & Biol.*, 34(4):647–654, 2008.

[19] S. H. Little, S.R. Igo, B. Pirat, M. McCulloch, C. J. Hartley, Y. Nosé, and W. A. Zoghbi. In vitro validation of real-time three-dimensional color Doppler echocardiography for direct measurment of Proximal Isovelocity Surface Area in mitral rigurgitation. *Am. J. Cardiol.*, 99(10):1440–1447, 2007.

[20] S.H. Little. Quantifying mitral valve regurgitation: new solutions from the 3rd dimension. *J. Am. Soc. Echocardiogr.*, 23(1):9–12, 2010.

[21] N.A. Marsan, F. Maffessanti, G. Tamborini, P. Gripari, E. Caiani, L. Fusini, M. Muratori, M. Zanobini, F. Alamanni, and M. Pepi. Left atrial reverse remodeling and functional improvement after mitral valve repair in degenerative mitral regurgitation: a real-time 3-dimensional echocardiography study. *Amer. Heart J.*, 161(2):314–321, 2011.

[22] S. Mishra and K. Jayaraman. Asymmetric flows in planar symmetric channels with large expansion ratios. *Int. J. Num. Meth. Fluids*, 38:945–962, 2002.

[23] H.K. Moffatt. Viscous and resistive eddies near a sharp corner. *J. Fluid Mech.*, 18:1–18, 1964.

[24] Rick A. Nishimura, Catherine M. Otto, Robert O. Bonow, Blase A. Carabello, John P. Erwin, III, Robert A. Guyton, Patrick T. OGara, Carlos E. Ruiz, Nikolaos J. Skubas, Paul Sorajja, Thoralf M. Sundt, III, and James D. Thomas. 2014 aha/acc guideline for the management of patients with valvular heart diseasea report of the american college of cardiology/american heart association task force on practice guidelines. *Journal of the American College of Cardiology*, 63(22):e57–e185, 2014.

[25] V.T. Nkomo, J.M. Gardin, T.N. Skelton, J.S. Gottdiener, C.G. Scott, and M. Enriquez-Sarano. Burden of valvular heart diseases: a population-based study. *Lancet*, 368:1005–11, 2006.

[26] M.S.N. Oliveira, L.E. Rodd, G.H. McKinley, and M.A. Alves. Simulations of extensional flow in microrheometric devices. *Microfluid Nanofluid*, 5:809–826, 2008.

[27] T. Passerini, A. Quaini, U. Villa, A. Veneziani, and S. Canic. Validation of an open source framework for the simulation of blood flow in rigid and deformable vessels. *International Journal for Numerical Methods in Biomedical Engineering*, 29(11):1192–1213, 2013.

[28] G. Pedrizzetti, G. LaCanna, O. Alfieri, and G. Tonti. The vortex–an early predictor of cardiovascular outcome? *Nature Reviews Cardiology*, 11:545–553, 2014.

[29] G. Pitton, A. Quaini, and G. Rozza. Computational reduction strategies for bifurcations and stability in fluid-dynamics: Applications to coanda effect. Numerical Analysis & Scientific Computing Preprint Series No. 54, Department of Mathematics, University of Houston, 2016.

[30] A. Quaini, S. Canic, R. Glowinski, S.R. Igo, C.J. Hartley, W.A. Zoghbi, and S.H. Little. Validation of a 3D computational fluid-structure interaction model simulating flow through an elastic aperture. *J. Biomech.*, 45(2):310–318, 2012.

[31] A. Quaini, S. Canic, G. Guidoboni, R. Glowinski, S.R. Igo, C.J. Hartley, W.A. Zoghbi, and S.H. Little. A three-dimensional computational fluid-dynamics model of regurgitant mitral valve flow: validation against in vitro standards and 3d color doppler methods. *Cardiovascular Engineering and Technology*, 2(2):77–89, 2011.

[32] A. Quaini, R. Glowinski, and S. Canic. Symmetry breaking and preliminary results about a Hopf bifurcation for incompressible viscous flow in an expansion channel. *International Journal of Computational Fluid Dynamics*, 30(1):7–19, 2016.

[33] A. Quarteroni, R. Sacco, and F. Saleri. *Numerical Mathematics*. Springer Verlag, 2007.

[34] A. Quarteroni, F. Saleri, and A. Veneziani. Analysis of the Yosida method for the incompressible Navier-Stokes equations. *J. Math. Pures Appl.*, 78:473–503, 1999.

[35] A. Quarteroni, F. Saleri, and A. Veneziani. Factorization methods for the numerical approximation of Navier-Stokes equations. *Comput. Methods Appl. Mech. Engrg.*, 188:505–526, 2000.

[36] A. Quarteroni and A. Valli. *Numerical Approximation of Partial Differential Equations*. Springer-Verlag, 1994.

[37] A. Revuelta. On the two-dimensional flow in a sudden expansion with large expansion ratios. *Phys. Fluids*, 17(1):1–4, 2005.

[38] F. Saleri and A. Veneziani. Pressure Correction Algebraic Splitting Methods for the Incompressible Navier-Stokes Equations. *SIAM Journal on Numerical Analysis*, 43(1):174–194, 2006.

[39] D.J. Tritton. *Physical Fluid Dynamics (Section 22.7, The Coanda Effect).* Van Nostrand Reinhold, 1977 (reprinted in 1980.

[40] Chien-Hsiung Tsai, Han-Taw Chen, Yao-Nan Wang, Che-Hsin Lin, and Lung-Ming Fu. Capabilities and limitations of 2-dimensional and 3-dimensional numerical methods in modeling the fluid flow in sudden expansion microchannels. *Microfluidics and Nanofluidics*, 3(1):13–18, 2007.

[41] R. Wille and H. Fernholz. Report on the first European mechanics colloquium on Coanda effect. *J. Fluid Mech.*, 23:801–819, 1965.

[42] W.A. Zoghbi, M. Enriquez-Sarano, E. Foster, P.A. Grayburn, C.D. Kraft, R.A. Levine, P. Nihoyannopoulos, C.M. Otto, M.A. Quinones, H. Rakowski, W.J. Stewart, A. Waggoner, and N.J. Weissman. American Society of Echocardiography: Recommendations for evaluation of the severity of native valvular regurgitation with two-dimensional and Doppler echocardiography. *Eur. J. Echocardiogr.*, 4:237–261, 2003.